Supplementary Information

Enhanced gamma-ray betatron radiation from laser accelerator and plasma radiator

M. Mirzaie[1※], K. H. Pae[1,2※], C. I. Hojbota[1,3※], S. Smartsev[4], S. Tata[4], Vishwa Bandhu Pathak [1, 5], D. Y. Kim[1], Y. J. Rhee[1], L. Bae[1,2], J. H. Sung[1,2], J. W. Yoon[1,2], S. K. Lee[1,2], T. Pak[1], J. H. Jeon[1], S. H. Cho[1], Chang Hee Nam[1,6], V. Malka[3†], and Hyung Taek Kim[1,2‡]

[1]*Center for Relativistic Laser Science, Institute for Basic Science, Gwangju, Korea,*
[2]*Advanced Photonics Research Institute, GIST, Gwangju, Korea,*
[3]*Department of Physics, The University of Texas at Austin, Austin, Texas, USA*
[4]*Department of Physics of Complex Systems, Weizmann Institute of Science, Rehovot, Israel*
[5]*School of Advanced Sciences, Vellore Institute of Technology, Vellore, Tamil Nadu, India*
[6]*Department of Physics and Photon Science, GIST, Gwangju, Korea*
[†]*victor.malka@weizmann.ac.il* and [‡]*htkim@gist.ac.kr*

1. Two gas target setup

Figure S1 illustrates the two-stage plasma target configuration for hybrid betatron gamma-ray generation and shows the neon supersonic gas jet's density distribution as measured by Mach–Zehnder interferometry. A gas jet with a 2-mm-diameter orifice was installed after the gas cell as a radiator. The center of the gas jet was located with a 5-mm gap from the exit of the gas cell. At this gap between the gas cell and the jet, we could avoid the effects of high-density puffing of the gas jet into gas cell medium, which can detune the condition for LWFA. Additionally, the location was carefully chosen to observe the effect of high-density neon jet on betatron radiation.

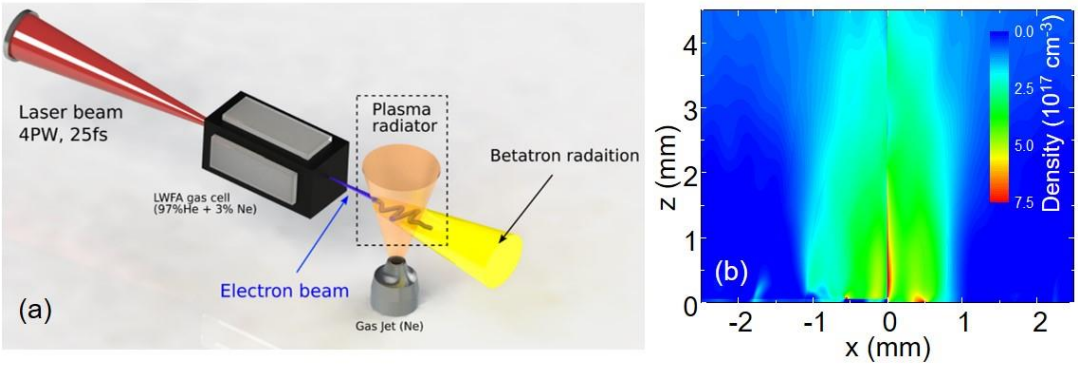

Fig. S1| (a) Two target geometries. A gas cell filled with He gas and 3% Ne as LWFA target, a high-density Ne gas jet, as a radiator enhancing the betatron signal. (b) Gas density profile of the Ne gas jet.

2. Gamma-ray detection setup

Figure S2.**a** presents photographs and the configuration of the radiography grid, composed of tungsten and stainless-steel elements, used to characterize hybrid betatron emission. Figure S2.**b** shows the angularly distributed metal filter wheel used for gamma-ray energy measurements.

Fig. S2| (a) A metallic structure, consisting of tungsten bars of varying thicknesses and stainless steel rings, was used for radiography and (b) an attenuation filter composed of different materials and thicknesses

3. PIC simulation of the LWFA for the first medium of a long plasma target

Figure S3 shows the simulation setup for the LWFA and betatron radiation from a single-stage gas cell. A laser pulse with normalized vector potential a_0 =3.0, a spot size of 45 μm, and a duration of 25 fs enters a 5 cm-long plasma target for LWFA and betatron radiation in a single gas-cell configuration. The azimuthal mode decomposition method is employed to simulate long-distance propagation[35]. The target plasma features a 4 cm flat-top region flanked by 5 mm $\sin^2$ ramp sections at both the entrance and exit.

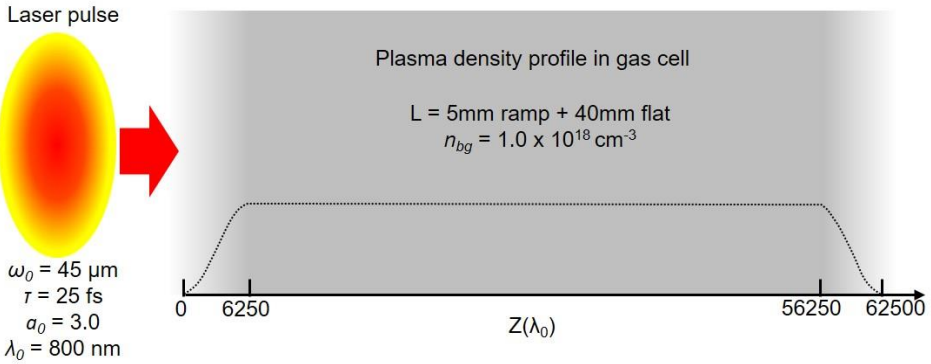

Fig. S3| PIC numerical simulation setup for the LWFA betatron radiation

Figure S4 presents PIC simulation results for the radiation density map, electron density, and longitudinal momentum along the laser propagation path. These results show that betatron emission is strong only in specific sections of the propagation where transverse electron motion is pronounced; however, the total radiated betatron flux in this stage is much smaller than that produced in the high-density radiator.

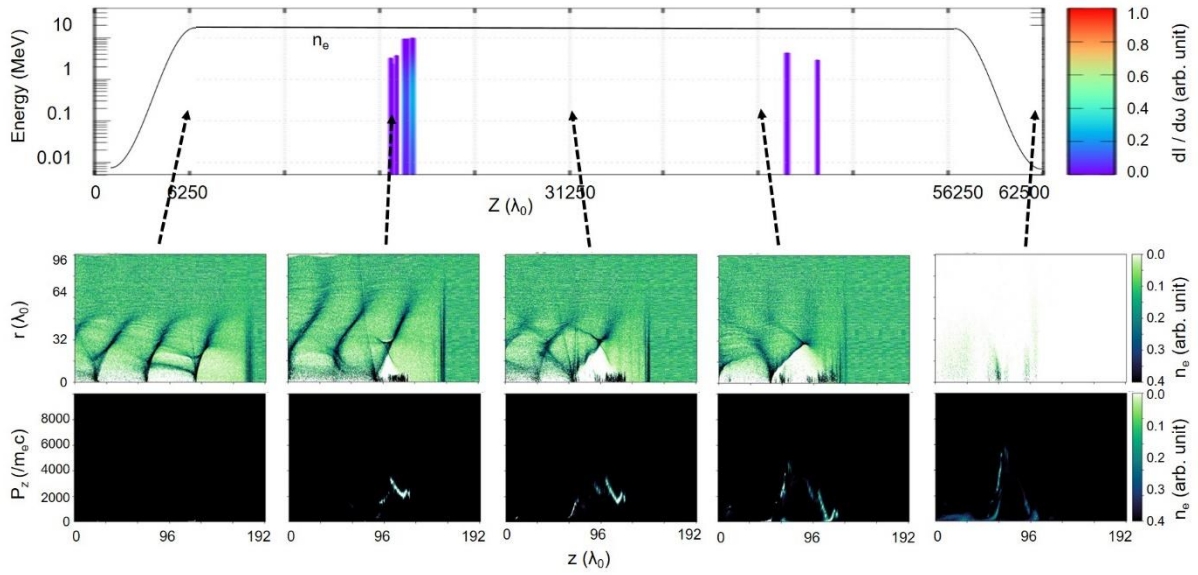

Fig. S4| Quasi-3D PIC numerical simulation result: (top) radiation density map, (middle) electron density, and (bottom) longitudinal momentum.

Figure S5 shows the electron beam spectrum after 3.5 cm of laser propagation, with the beam energy distributed in the 1–2 GeV range and a total charge above 100 MeV of approximately 200 pC. These results demonstrate that the experimental observations and the assumed beam parameters entering the second plasma stage are well corresponding to the PIC simulation outcomes from the single-stage gas cell simulation.

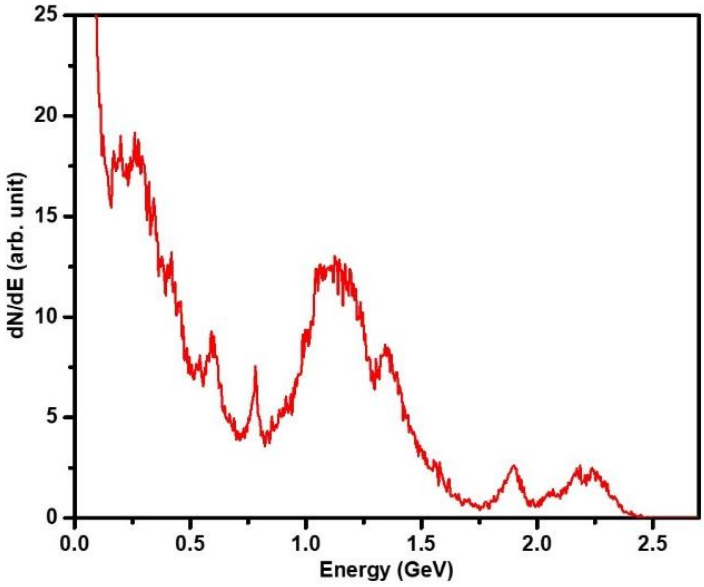

Fig. S5| PIC simulation result of the electron spectrum accelerated from the LWFA stage at z = 3.5cm. Total charge above 100 MeV is about 200 pC.

4. Simulations for the 2nd medium of a short high density plasma

For the second-stage radiator simulations, we preset the laser, electron-beam, and plasma parameters based on experimental observations and PIC results from single-stage LWFA in the gas cell, as illustrated in Fig. S6. A residual laser pulse emerging from the first stage, with normalized vector potential a_0 =1.0, 48 μm spot size, and 25 fs duration, enters the electron plasma of the second stage. This pulse is followed by an electron beam carrying 200 pC charge at a central energy of 1.0 GeV, with a bunch length of 10 μm and a radius of 5 μm. The target plasma profile features a peak electron density in the range 10^{19}–10^{20} cm^{-3}, with no flat-top region and sin² ramps of 1.75 mm at both the leading and trailing edges. The azimuthal mode decomposition method[35] is employed.

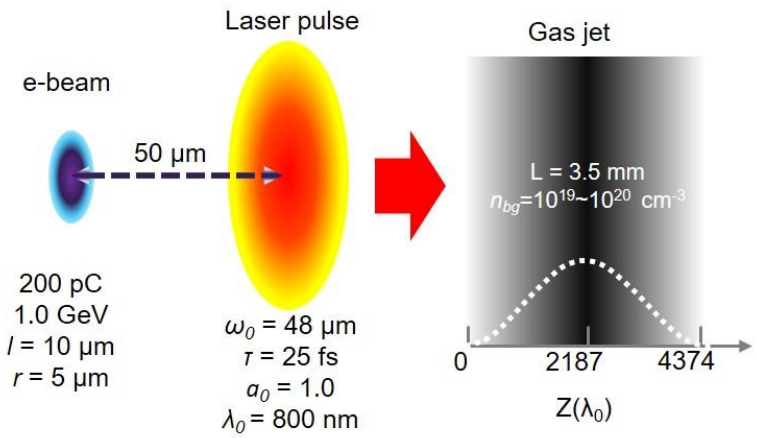

Fig. S6| Schematics of the quasi-3D PIC numerical simulations for 2-stage configuration.

Figure S7 shows the electron-beam trajectory distributions at the points of maximum betatron emission for both low- and high-density cases, based on the distance–energy correlation in Fig. 5. In the lower panels of Fig. S7, regions of strong betatron emission coincide with pronounced transverse oscillations. In the high-density case, these oscillations occur at a relatively short propagation distance—before significant energy depletion—yielding larger amplitudes. In contrast, for the low-density plasma, transverse oscillations appear only after the density peak has passed and the beam has undergone considerable depletion, resulting in weaker oscillations. This explains the stronger betatron radiation in the high-density scenario.

These findings indicate that optimizing the radiator's density profile and length could further enhance betatron emission.

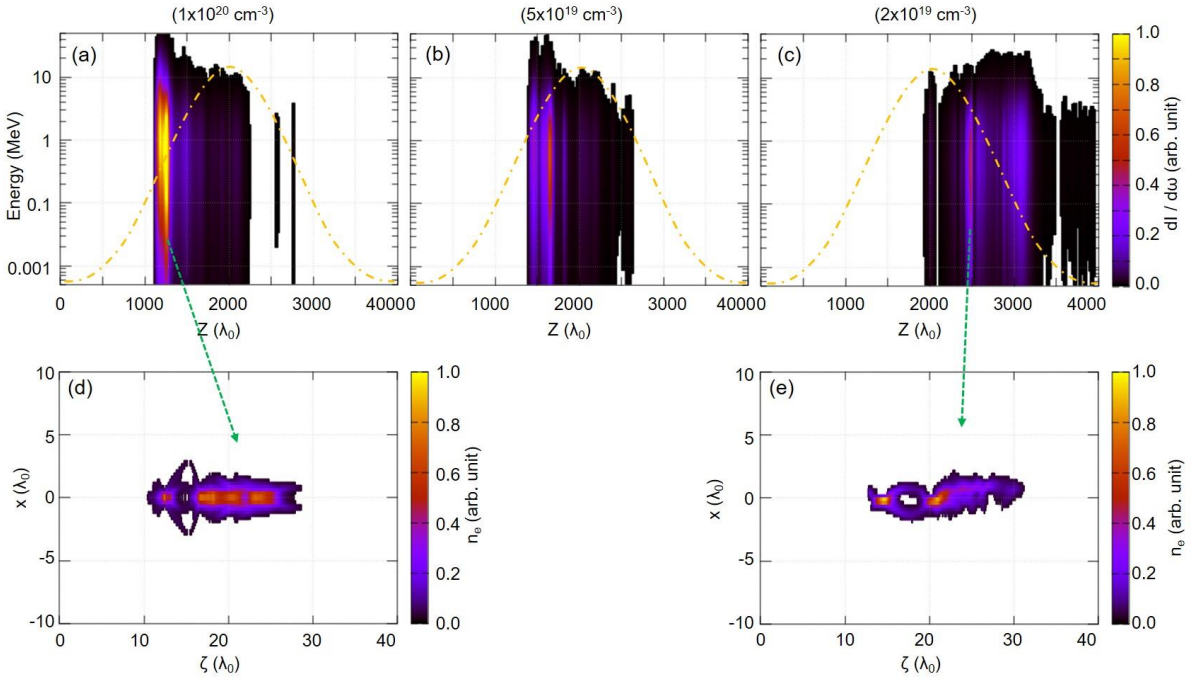

Fig. S7| Betatron radiation density maps are shown on a linear scale for background electron densities of (a) 1×10^{20} cm^{-3}, (b) 5×10^{19} cm^{-3}, and (c) 2×10^{19} cm^{-3}. Electron beam density maps in z-x space at the locations of the strongest radiation emission for the cases (d) $n_{bg}=1\times10^{20}$ cm^{-3} and (e) $n_{bg}=2\times10^{19}$ cm^{-3}.